Materials Advances

ROYAL SOCIETY OF CHEMISTRY

PAPER

View Article Online
View Journal | View Issue

Check for updates

Cite this: *Mater. Adv.*, 2020, 1, 774

Received 22nd April 2020,
Accepted 24th May 2020

DOI: 10.1039/d0ma00231c

rsc.li/materials-advances

Peroxidase-like behavior and photothermal effect of chitosan-coated Prussian-blue nanoparticles: dual-modality antibacterial action with enhanced bioaffinity†

Nayanika Chakraborty,[a] Diksha Jha,[b] Hemant K. Gautam*[b] and Indrajit Roy *[a]

We have probed the antibacterial potential of Prussian blue nanoparticles, without (PB) and with (CHPB) chitosan-coating. Both these nanoparticles showed peroxidase-like behavior by degrading hydrogen peroxide and generating toxic reactive oxygen species (ROS). The nanoparticles also showed a photothermal effect by generating heat (hyperthermia) upon activation with 635 nm laser light. The antibacterial activity resulting from the combined peroxidase-like behavior and photothermal effect of these nanoparticles was explored in both Gram-positive and Gram-negative bacteria. It was observed that CHPB nanoparticles showed much higher antibacterial activity than PB nanoparticles, which is attributed to the favorable electrostatic interaction at the nanoparticle–bacteria interface upon chitosan coating. Further light activation led to enhanced antibacterial action, with near-complete bacterial cell death observed at CHPB treatment concentrations of 75 μg ml^{-1} for Gram-negative bacteria and 125 μg ml^{-1} for Gram-positive bacteria. The mechanism of antibacterial action of the nanoparticles was also explored though a series of assays, such as electron microscopic analysis of nanoparticle–bacteria binding, membrane depolarization, protein leakage, intracellular ROS generation, *etc.* Based on these studies, we conclude that CHPB nanoparticles act as robust dual-modality antibacterial agents with enhanced affinity at the nanoparticle–bacteria interface.

Introduction

A major problem in modern healthcare is the widespread emergence of multidrug-resistant (MDR) bacterial strains, making most traditional antibiotics ineffective for the treatment of bacterial diseases.[1–3] Therefore, researchers worldwide are focusing on the use of certain nanoparticles with inherent antibacterial potential as attractive alternatives for controlling bacterial diseases and biofilm formation.[4–6] Nanoparticles have a high surface-to-volume ratio and surface energy, and can incorporate desired functional groups, biomaterials, or active agents such as antibiotics, chemotherapy drugs, and biopolymers.[7,8] These properties facilitate their desired interaction and manipulation of biological systems. Nanoparticles are also known to be influenced by external forces, such as light and magnetic fields, providing additional therapeutic possibilities.[9,10] Therefore, it is expected that nanoparticles will play a major role in combating bacterial infections in the near future.

Though identification of the various modes of antibacterial action of nanoparticles is still an evolving area of research, a few early trends have been recognized. Silver-based nanoparticles have been extensively used to treat bacteria owing to their ability to generate reactive oxygen species (ROS) and cause silver-ion mediated toxicity.[11–13] However, the high cost, nonspecific toxicity, uncontrolled leaching of Ag$^+$ ions, and evidence of antibacterial resistance make their widespread use difficult.[14–16] Certain nanoparticles are known to manipulate oxidative processes by mimicking key enzymes, such as oxidase and peroxidase.[17,18] Such nanoparticles, called nanozymes, have been explored recently as antibacterial agents owing to their ability to generate toxic intracellular ROS.[19,20] Some nanoparticles, which produce localized heating (hyperthermia) when excited with visible-near infra-red (NIR) light, are being used in antibacterial photo-activated therapies.[21,22] These

---

[a] *Department of Chemistry, University of Delhi, India. E-mail: indrajitroy11@gmail.com*
[b] *Institute of Genomics and Integrated Biology, Sukhdev Vihar, Delhi 110025, India. E-mail: hemant@igib.res.in*

† Electronic supplementary information (ESI) available: TGA profile of CHPB NPs, EDX spectra of PB and CHPB NPs, 2D AFM images of PB and CHPB NPs along with the same field 3D AFM images, peroxidase-like activity of PB and CHPB NPs, the growth kinetics curves for PA and SA with PB and CHPB NPs with and without irradiation, colony counting (CFU) assay, MIC experiment performed against *P. aeruginosa* with chitosan only, TEM analysis of nanoparticle–bacteria interaction, and cytotoxicity of CHPB NPs against HEK-293 cells. See DOI: 10.1039/d0ma00231c

exciting developments have triggered the quest for the development of ideal nanoparticulate systems with low non-specific toxicity but robust antibacterial action.

Prussian blue (PB) nanoparticles are biocompatible, cost effective and clinically approved mixed valence iron hexacyanoferrates, with the general formula $Fe_4[Fe(CN)_6]_3$.[23,24] They are also known to behave as an enzyme peroxidase, with applications in sensing, oxidative modulation, *etc.*[25,26] Moreover, these nanoparticles have broad band optical absorption in the visible and NIR window, with high molar extinction coefficients and photothermal conversion efficiency. As a result, they are promising agents for photothermal therapy (PTT) for the treatment of several diseases, including cancer and bacterial infections.[27–29] Maaoui *et al.* reported that PB NPs coated with polyvinyl pyrrolidone (PVP), in combination with near infra-red (980 nm) laser irradiation, can be used for the robust ablation of virulent Gram positive and Gram negative bacterial strains.[30] However, mechanistic details related to their interaction with the bacterial cells were not provided. Moreover, the combined antibacterial potential arising from the peroxidase-like activity and photothermal effect of PB NPs has not yet been reported in the literature.

In this work, we have explored the dual modality (peroxidase like ROS generation and photothermal) antibacterial activity of chitosan-coated PB (CHPB) nanoparticles. Coating with the biocompatible and bioadhesive polymer chitosan has been carried out to facilitate the interaction of the nanoparticles at the nanoparticle–bacteria interface.[31] Similar chitosan-coating strategies have been reported to enhance the antibacterial efficiency of several other nanoparticles, such as that of iron oxide and gold.[32–34] Chitosan is known to interact with the cyanoferrate groups on the PB surface to produce stable PB (core)/chitosan (shell) NPs, which have already been applied in several areas, such as electrocatalysis, photo-triggered gene delivery, photothermal therapy, *etc.*[35–38] We report for the first time the dual modality antibacterial application of CHPB NPs against both Gram-negative bacteria, *Pseudomonas aeruginosa*, and Gram-positive bacteria, *Staphylococcus aureus*. We investigated in detail the antibacterial mechanism using assays for peroxidase activity, intracellular ROS generation, cell viability, *etc.*, without and with light activation. The affinity of NPs for the bacterial surface caused membrane damage, disruption in the cell permeability and an increase in production of ROS, leading to cell death. The study was extended to probe the role of light-activated photothermal therapy in the mechanism, which enhanced the overall antibacterial propensity of the NPs.

Experimental section

Materials

Potassium hexacyanoferrate(II) trihydrate, $K_4Fe(CN)_6{\cdot}3H_2O$, 98%, was obtained from SRL. Anhydrous iron(III) chloride ($FeCl_3 \geq 97\%$) was obtained from Merck. Acetone was purchased from CDH (P) Ltd India. Low molecular weight Chitosan (with 75% degree of deacetylation), acetic acid, *o*-dianisidine (DA), propidium iodide, Bradford reagent and 2,7-dichlorofluoroscein diacetate (DCFH-DA) were purchased from Sigma Aldrich. Resazurin sodium salt was purchased from TCI Co. Ltd India. Mueller-Hinton broth (MHB) growth media and ethanol were purchased from Merck. All reagents were used as received.

Synthesis of chitosan-coated PB nanoparticles

The cationic biopolymer chitosan is water soluble at a pH below its pK_a value range (between 6.2 and 6.8) owing to extensive protonation of its free amine groups.[31] Chitosan coated PB (CHPB) NPs were synthesized in a two-step process in accordance with previous reports, with some modifications.[35,36] The first step involved a strong electrostatic interaction between hexacyanoferrate ions (20 ml of 1 μM aqueous solution of potassium hexacyanoferrate) and acidified chitosan solution (80 ml of 0.025% w/v chitosan solution in 0.2% aqueous acetic acid) at room temperature for 30 minutes with constant magnetic stirring, resulting in the formation of a stable whitish dispersion. After that, an aqueous solution of ferric chloride was added dropwise (20 drops per min) into the mixture under constant stirring, leading to the formation of CHPB NPs (indicated by a dark-blue colored solution). To purify the as-synthesized NPs, 30 ml of acetone was added to 10 ml of the reaction mixture. The obtained precipitate was centrifuged, followed by multiple washing cycles with acetone. This process removes free chitosan and other unreacted reagents from the NPs. The precipitated NPs were re-dispersed into acidified water with the help of a probe sonicator for 15 minutes. The solution was further allowed to precipitate with the addition of acetone, followed by centrifugation. Uncoated PB NPs (control) were also prepared using a similar protocol. Aqueous $K_3Fe(CN)_6$ (1 mM) was mixed with an equimolar aqueous solution of $FeCl_3$. The resulting precipitate of PB was purified and redispersed similarly to the process described for CHPB NPs.

Characterization of the NPs

A UV-1601 Spectrophotometer (Shimadzu, Japan) was used to record the optical properties of the CHPB and PB NPs in the wavelength range of 400–900 nm. For fluorescence measurements, a Cary Eclipse Fluorescence Spectrophotometer was used. Fourier transform infrared (FT-IR) spectral measurements were performed using a PerkinElmer RXI FTIR spectrometer at a resolution of 4 cm^{-1} to analyze surface functionality. X-ray powder diffraction (XRD) data were collected using a 3 kW Bruker D8 Discover X-ray powder diffractometer with monochromatized Cu Kα radiation (λ = 1.54 A). A PerkinElmer SII thermal gravimetric analysis (TGA) instrument was used to study the thermal degradation profile of the CHPB and PB nanoparticles, along with pure chitosan. The analyzed samples were heated in a temperature range of 10–600 °C with a heating rate of 10 °C min^{-1} under a constant nitrogen flow. Raman spectra were recorded using a LabRAM HR evolution Raman spectrometer with a Horiba laser of wavelength 785 nm. Transmission electron microscopy (TEM) operating at an accelerating voltage of 300 kV (TECNAI G^2 T-30) was used to identify the size and morphology of the nanoparticles. The surface analysis was done using Solver Model, NTMDT (Russia) atomic force microscopy (AFM) with three dimensional visualization. The surface charge (zeta potential) and hydrodynamic size of the CHPB and PB NPs were measured using a Zetasizer Nano ZS instrument (Malvern, UK).

Determination of peroxidase-like activity of the NPs

The enzyme peroxidase acts on the substrate (H_2O_2) to produce short-lived reactive oxygen species (ROS), which oxidizes several other reagents.[39] We investigated the peroxidase-like activity of the PB and CHPB NPs using the chromogenic reagent *o*-dianisidine (DA). DA is oxidized by the generated ROS to an orange-brown colored solution with a peak wavelength of 430 nm, which is measured spetrophotometrically.[21,39] The oxidation of DA at a constant concentration of 0.0315 M was observed at room temperature using phosphate buffer (pH 7.2) in the presence of PB and CHPB NPs (50 μg ml^{-1}) for 20 minutes. The reaction was started with the addition of H_2O_2 (1 M, 100 μl) to the reaction system. The catalyzing property of the nanoparticles was carefully monitored using a UV-visible spectrophotometer.

Photothermal effect and photothermal stability

To monitor the photothermal effect, aqueous dispersions of the PB and CHPB NPs (3 ml of Millipore water, 100 μg ml^{-1} each) were subjected to irradiation (for 10 minutes) with a continuous wave laser with an emission wavelength of 635 nm having 38 mW cm^{-2} power density. The temperature variation was recorded using a digital thermocouple. The photostability of CHPB NPs was investigated by irradiating the NPs (laser on) and subsequent cooling (laser off) for a period of ten minutes, continuously for four cycles, and recording the temperature variation using a digital thermocouple.

Antibacterial studies involving the NPs

In this study, the bacterial strains used were Gram positive *Staphylococcus aureus* (*S. aureus*) (MTCC 740) and Gram negative *Pseudomonas aeruginosa* (*P. aeruginosa*). The preparation of cultures for both the bacterial strains involved taking loop full bacteria from the respective slant cultures and growing them in Mueller-Hinton broth (MHB) medium at an optimum temperature of 37 °C with constant agitation at 180 rpm for 12 hours.

Primarily, the effects produced due to the interaction of the synthesized PB and CHPB NPs with *S. aureus* and *P. aeruginosa*, with and without light activation, were analyzed by following their growth kinetics. Bacteria were grown in fresh MHB media in 24-well plates, and treated with aqueous dispersions of escalating dosages of PB and CHPB NPs for 12 hours. The untreated cells were taken as the growth control. The treated cells were irradiated with laser light for a time duration of 7 minutes by placing a diode laser (wavelength of 635 nm, power density of 38 mW cm^{-2}) vertically downward to focus the beam on a particular well. The plates were incubated following completion of nanoparticle treatment, without and with laser irradiation. A periodic analysis of the growth of the untreated and treated cells was achieved by measuring their optical density (O.D.) at 600 nm using a spectrophotometer at regular intervals of incubation time (0, 4, 8 and 12 hours).

Micro broth dilution assay was performed to check the minimum inhibitory concentration (MIC) of the PB and CHPB NPs against the bacteria *S. aureus* and *P. aeruginosa* in a sterile 24 well cell culture plate. Briefly, 25 μl of bacterial cultures was added to the wells containing increasing concentrations of nanoparticles. The total volume in each well was maintained at 500 μl by adding Mueller-Hinton broth. The wells were irradiated for 7 min each by 635 nm diode laser with a power density of 38 mW cm^{-2}. An equal number of wells were measured without laser irradiation. After 12 hours of incubation, the growth of the cells was monitored by measuring the absorbance at 600 nm in a microplate reader (Tecan Infinite M200 Pro).

Assays to determine the antibacterial mechanism of the NPs

Four biochemical assays were performed on the bacterial cells: treated with CHPB NPs, with and without light exposure (635 nm diode laser). The treatment concentrations for the NPs were 25 μg ml^{-1} (MIC value) and 125 μg ml^{-1} (5× MIC value) for *P. aeruginosa*, and 75 μg ml^{-1} (MIC value) and 375 μg ml^{-1} (5× MIC value) for *S. aureus*. For comparison, the cells were also treated with uncoated PB NPs at their MIC and 5× MIC values. The control cells did not receive any treatment. The assays are:

(A) The ROS generation assay: ROS generation was measured using the broad-spectrum ROS sensitive fluorogenic dye DCFH-DA. After diffusion into the cell, DCFH-DA is deacetylated by cellular esterases to a non-fluorescent compound, which is later oxidized by ROS into 2′,7′-dichlorofluorescein (DCF), which is detected by fluorescence spectroscopy with excitation/emission wavelengths at 485 nm/535 nm.[40] The fluorescence output is proportional to the intracellular ROS generation. SA and PA were grown in MHB media till OD_{600} = 0.5 and then 1 ml was transferred into Eppendorf tubes and centrifuged at 1500 rpm. Later, it was washed with 1× PBS (pH 7.4) and treated with the NPs, with and without subsequent laser light irradiation. It was then incubated for 6 hours at 37 °C. The samples in Eppendorf tubes were centrifuged, washed with 1× PBS and treated with 100 μl of DCFH-DA (10 μM) for 30 min in the dark. Fluorescence spectra were recorded after incubation using a microplate reader (Tecan Infinite M200 Pro).

(B) Cell metabolism assay: the resazurin assay, also known as Alamar blue assay, offers a simple, rapid, and sensitive measurement for the viability of bacterial cells. Living cells are metabolically active and can reduce the nonfluorescent dye resazurin to the strongly-fluorescent resorufin *via* mitochondrial reductase.[41] The fluorescence output is proportional to the number of viable cells over a wide concentration range. This assay was performed according to the procedure mentioned above. After treatment with the NPs, the bacterial cells were washed with 1× PBS, supplemented with 50 μl of resazurin (5 μg ml^{-1}) and incubated in the dark for 30 min. Fluorescence spectra were recorded at 560/590 nm (excitation/emission wavelengths).

(C) Protein leakage assay: the Bradford protein assay is a rapid and precise bioanalytical procedure employed to determine the total concentration of leaked protein from the bacterial cells after treatment with increasing concentrations of CHPB and PB NPs. After NP treatment of the bacterial cells followed by centrifugation, the Bradford reagent was added to the cell-free supernatant and incubated for 5 minutes at 37 °C, after which the absorbance was measured at a wavelength of 595 nm. The observed absorbance is attributed to the stable complex formation between leaked protein and the Bradford reagent.[42] (D) Cell membrane integrity assay: propidium iodide (PI) uptake is one of the efficient methods used to evaluate cell membrane integrity due to the action of the NPs at the nano–bio interface.[43] The treated and untreated bacterial cell pellets were incubated at 37 °C with 15 μM fluorogenic dye (PI) for 30 minutes. Following this, the stained bacterial cells were washed and re-dispersed in PBS. PI is a membrane impermeant dye that can only fluoresce with compromised bacterial cell membranes at an excitation/emission wavelength of 535/617 nm. The observed fluorescence measurement gave an indication of the membrane integrity of the studied bacterial cells.

Transmission electron microscopy (TEM) analysis of NP-treated bacterial cells

The membrane damage and cellular morphology changes of SA and PA due to their interaction with PB and CHPB NPs, without and with light activation, were observed using TEM. The bacterial cells were treated with PB and CHPB NPs at their respective MIC values for a duration of 6 hours at 37 °C and shaking at 180 rpm. Half of the treated cells underwent laser light irradiation (635 nm, 38 mW cm^{-2}, 7 min). After treatment, the cells were washed with PBS twice, fixed with 4% paraformaldehyde (PFA) and incubated overnight at 4 °C. The fixed cells were then dehydrated with a graded ethanol series (15%, 25%, 35%, 45%, 55%, 75% and 95%) for 10 minutes each, drop casted on carbon-coated copper grids, stained with 1% uranyl acetate and imaged by TEM.

Results and discussion

Characterization of synthesized nanoparticles

The XRD profiles of both synthesized PB and CHPB NPs (Fig. 1A) showed multiple sharp diffraction peaks corresponding to the signature face-centered cubic (FCC) lattice of Prussian blue.[23,24] For CHPB NPs, the diffraction peak of Prussian blue at $2\theta \sim 17.6°$ of the (200) plane was observed, albeit with reduced intensity and some broadening, which is attributed to the surface coating with chitosan. Additionally, the analysis revealed that the other peaks at 2θ values of 24.7° (220) and 36.4° (400) were common for both cases, suggesting that the surface coating with chitosan does not significantly alter the typical FCC crystal structure of PB.

Furthermore, the successful validation of the chitosan coating on PB was deduced through Raman spectroscopy (Fig. 1B). Here, PB NPs showed a characteristic vibrational band at 2154.9 cm^{-1}.[44] This intense band is a result of a strong stretching vibration of the triple bond of the cyanide group present in PB NPs. CHPB NPs showed the same characteristic Raman peak as that of PB NPs, albeit with reduced intensity and a shift towards slightly higher energy (at 2155.3 cm^{-1}), thus indicating polymer coating on the nanoparticle surface.

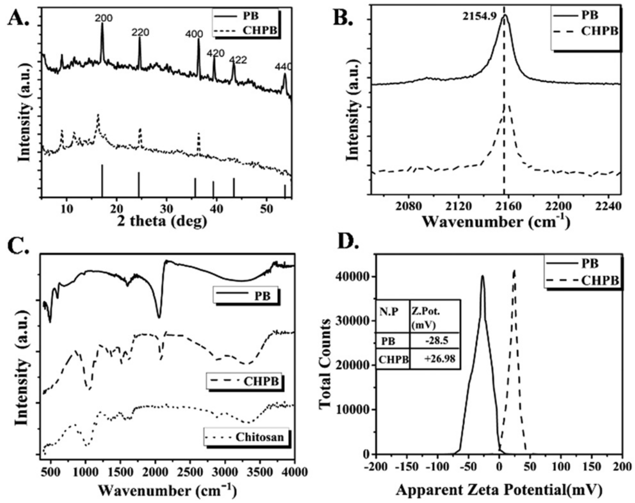

Fig. 1 Characterization of PB and CHPB NPs: (A) powder XRD profile, with simulated FCC profile at the bottom, (B) Raman spectra, (C) FTIR spectra, along with that of chitosan, and (D) zeta potential analysis.

The FTIR spectrum (Fig. 1C) of only chitosan showed a hump around 3000–3600 cm^{-1}, which originated from the stretching vibrations of N–H and O–H.[33] This signal shifted towards a lower frequency in the spectrum of the CHPB NPs, suggesting interaction of these functionalities with the PB nanocore. The characteristic peaks of chitosan at 1646 cm^{-1} for the acetamide group and 1524 cm^{-1} for the free amino group can also be observed in the CHPB NP spectrum. These peaks are absent in the spectrum of uncoated PB NPs. There is a slight shift of these IR peaks towards a lower frequency in the spectrum of the CHPB NPs, indicating the electrostatic interaction of free NH_2 groups of the chitosan molecule with the negatively charged PB surface. In the chitosan spectrum, the peak centered around 1032 cm^{-1} originated from C–O–C backbone stretching; this peak shifted towards a higher frequency with reduced intensity and broadness for the CHPB NPs, and it was absent for the uncoated PB NPs. In the PB NP spectrum, the very intense peak centered around 2061 cm^{-1} can be attributed to the C$\equiv$N stretching of the Fe(II)–CN–Fe(III) bond.[45] This characteristic peak is also evident for the CHPB NPs, but it shifted towards a higher frequency of 2086 cm^{-1} with reduced intensity. The reduction in the intensity of the cyanide peak for the CHPB NPs may be due to a decrease in population of the cyanide bond in the CHPB NPs compared to the uncoated PB NPs. In accordance with Hooke's law, the shift towards a higher frequency for the CHPB NPs indicates a more stable coordination of Fe(II)–CN–Fe(III) due to the steric environment provided by chitosan, which blocks the coordination of water molecules with ferric centers.[33] The absence of the peak at 590 cm^{-1} due to Fe–O stretching in the CHPB spectrum reinforces the above observation.

Surface charge (zeta-potential) measurement of CHPB NPs further validated the presence of chitosan on the surface of PB. The zeta potentials of CHPB and PB NPs were measured to be (+) 26.98 mV and (−) 28.5 mV, respectively (Fig. 1D). The reversal of surface charge of PB upon coating with chitosan is due to the cationic nature of chitosan, which masks the negatively charged cyanoferrate groups on the PB surface.

Moreover, the thermal degradation profile (TGA data) for uncoated PB, chitosan and the CHPB NPs (Fig. S1, ESI†) supported the FT-IR and XRD results. The TGA curve of uncoated PB showed a gradual weight loss, where degradation is caused due to two reasons: (i) the loss below 200 °C is due to the release of coordinated or zeolitic water and (ii) decomposition of PB to iron oxide. Chitosan showed a gradual loss of weight from 250 °C to 600 °C. Below 150 °C, the loss of water of crystallization can be observed. The thermal decomposition profile of the CHPB NPs is very similar to that of chitosan, showing a gradual loss of weight from 250 °C to 600 °C. Based on TGA data and the weight of the CHPB NPs before and after the measurements, the percentage of chitosan present on the CHPB NPs was estimated to be 24.0 ± 0.36% (w/w).

Fig. 2A and B TEM images of the CHPB NPs. The image of the CHPB NPs shows a spherical morphology and reasonable monodispersity, with an average diameter of 54.28 nm. The high resolution TEM image (Fig. 2B) of the CHPB NPs indicating the coating of chitosan over the PB core. The TEM data are supported by the DLS plot for PB and CHPB NPs (Fig. 2C). The lower hydrodynamic diameter of CHPB than PB NPs indicated that the crystal growth of PB is restricted upon chitosan coating.

Energy dispersive X-ray spectroscopy (Fig. S2, ESI†) was used to obtain the elemental identification and compositional analysis of the samples. Herein, we observed that the weight of iron is reduced by 3.73%, whereas there is an increase of 38.13% for carbon in CHPB, indicating the successful coating of chitosan over the PB nanocore.

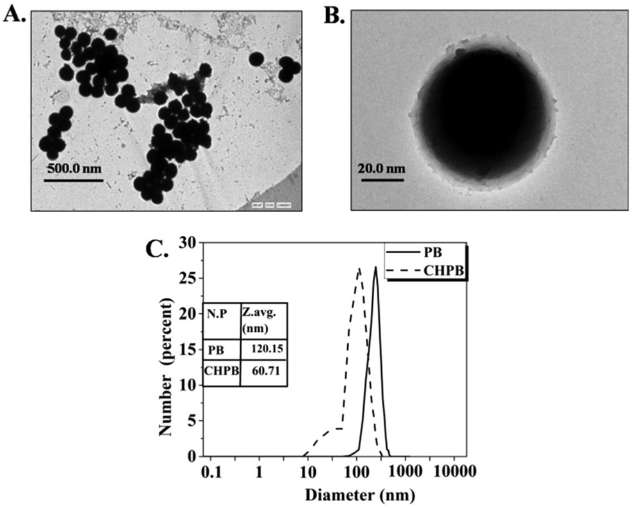

Fig. 2 Size and morphological characterization of the nanoparticles. (A and B) TEM image of CHPB NPs at a scale of (A) 500 nm and (B) 20 nm, showing surface coating of chitosan on the PB core. (C) Comparative DLS data of PB and CHPB NPs.

Atomic force microscopy (Fig. S3, ESI†) analysis was carried out to determine the change in surface topography when chitosan is coated on the PB surface. The root mean square (rms) surface roughness is greater for PB NPs than for CHPB NPs, indicating the polymeric coating of the CHPB NPs. A spherical morphology can also be observed in the 2D AFM images of the CHPB NPs, thus validating the TEM data.

Peroxidase-like activity of PB and CHPB NPs

Recent studies have shown the potential of some nanoparticles to behave as an enzyme peroxidase, whereby they reduce peroxide to produce reactive oxygen species (ROS), which may be used to kill bacteria *via* oxidative damage of important biomolecules.[19–22] Fig. 3A shows that both the nanoparticles produced a colored solution in the presence of hydrogen peroxide and *o*-dianisidine (DA), whereas no color change was observed in the absence of the nanoparticles. This data demonstrate that both these nanoparticles convert H_2O_2 to highly reactive ROS with peroxidase-like activity. Fig. 3B shows the time-dependent enhancement in ROS production (indicated by an increase in optical density at 430 nm) of both PB and CHPB NPs up to a period of 20 minutes. It may be noted that PB or CHPB NPs themselves have poor absorption coefficients in this wavelength range, and therefore did not interfere with this colorimetric assay. The peroxidase-like catalyzing property of CHPB and PB NPs can be attributed to the ferrous centers, which can interact with the substrates to participate in various redox reactions.

To study the time-dependence of this catalytic activity, a steady state kinetics experiment varying the concentration of the substrate H_2O_2, at a fixed concentration of DA, was carried out at room temperature. The typical Michaelis–Menten curves were obtained for both PB and CHPB NPs (Fig. S4, ESI†). From the corresponding Lineweaver–Burk plots, the apparent V_{max} and K_{m} values for PB and CHPB NPs were obtained. V_{max} and K_{m} values for PB NPs were found to be 3.662 μM min^{-1} and 2.947 mM, respectively, whereas for CHPB NPs, the values were 5.109 μM min^{-1} and 4.363 mM, respectively.

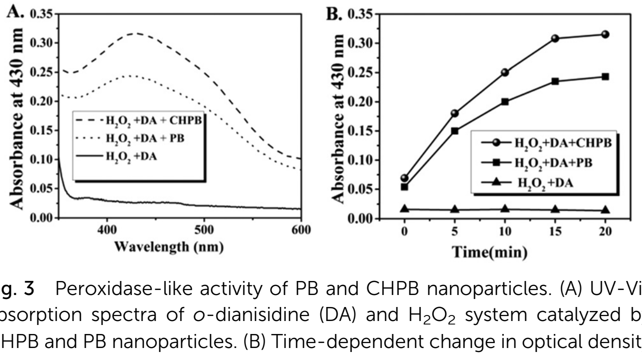

Fig. 3 Peroxidase-like activity of PB and CHPB nanoparticles. (A) UV-Vis absorption spectra of *o*-dianisidine (DA) and H_2O_2 system catalyzed by CHPB and PB nanoparticles. (B) Time-dependent change in optical density (at a peak wavelength of 430 nm), showing catalyzing properties of PB and CHPB nanoparticles with H_2O_2 as the substrate, at a constant concentration of DA.

Optical and photothermal properties of PB and CHPB NPs

Fig. 4A shows the UV-Vis absorption spectra of chitosan, PB and the CHPB NPs. The absorption bands of both PB and CHPB NPs exhibited characteristic broad bands covering the visible and NIR regions, corresponding to inter-metal charge transfer from Fe^{2+} to Fe^{3+}, with λ_{max} values close to 700 nm. The λ_{max} of CHPB NPs is located at a slightly shorter wavelength (4 nm blue shift) than that of PB NPs. This observation is consistent with previous reports, suggesting interaction between the PB nanocore and the polymer coating.[46]

The photothermal data for the aqueous dispersions of the PB and CHPB NPs are given in Fig. 4B. The temperature rise in the case of water (control) was only 2.5 °C under the same irradiation conditions. On the other hand, a substantial increase in temperature was observed for both PB and CHPB NPs, with ΔT values of 12.9 °C and 13.6 °C, respectively. The photostability data of CHPB NPs (Fig. 4C) displayed a negligible decrease in the maximum temperature attained by the NPs, demonstrating their robust photothermal stability. The reasonably high absorbance coefficient, substantial photothermal effect and good photothermal stability observed with a low power laser make both PB and CHPB NPs potentially attractive biocompatible nano-devices for photothermal therapy (PTT).

Antibacterial activity of PB and CHPB NPs

The photoactivated antibacterial potential of PB and CHPB NPs was ascertained by treating *P. aeruginosa* and *S. aureus* bacterial cells with various dosages of these nanoparticles, without and with laser subsequent irradiation with laser (continuous wave laser emitting at 635 nm, with a power density of 38 mW cm^{-2}). The data, presented in Fig. 5A–D, show an enhanced antibacterial effect on increasing the concentration of the nanoparticles in the dark (without laser), which further increased for each dosage upon laser irradiation. Upon comparing the effects of PB and CHPB NPs, it is evident that the growth inhibition potential of CHPB NPs (Fig. 5A and C) is always higher than that of PB NPs (Fig. 5B and D), under both dark (without laser) and light (with laser) conditions, for both the bacteria tested. This indicated that CHPB NPs have a higher antibacterial potential than PB NPs for both Gram-negative and Gram-positive bacteria. Moreover, it is also worth noting that the two bacteria showed different sensitivities towards CHPB NPs, with the Gram-negative *P. aeruginosa* being more sensitive than the Gram-positive *S. aureus*.

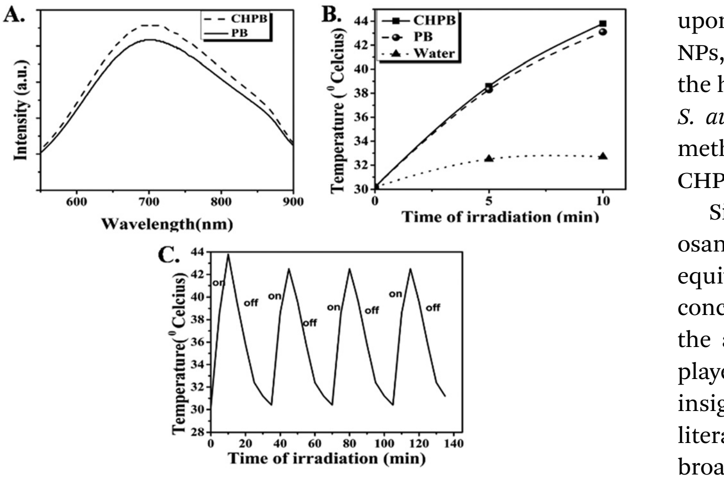

Fig. 4 (A) Absorption spectra of PB and CHPB NPs. (B) Temperature variation in 100 μg ml^{-1} aqueous dispersions of PB and CHPB NPs upon irradiation for 10 minutes with a laser of 635 nm. (C) Photostability of CHPB NPs: temperature variation of CHPB NPs upon repeated laser irradiation over four consecutive heating (laser on)–cooling (laser off) cycles (10 minutes of irradiation for each cycle).

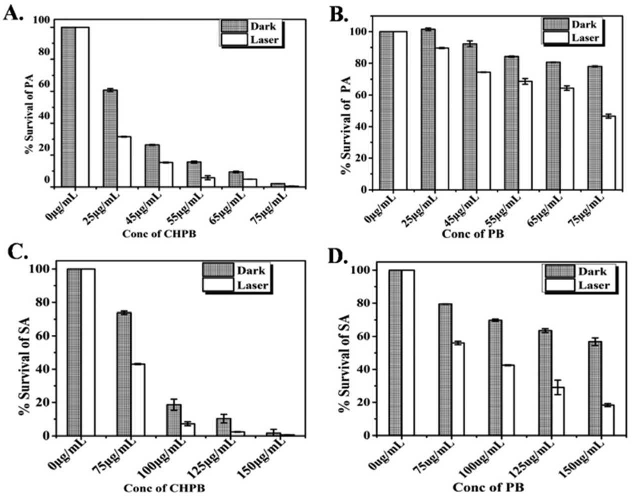

Fig. 5 Antibacterial activity of PB and CHPB NPs. (A and B) Treatment of *P. aeruginosa* (PA) with increasing concentrations of (A) CHPB and (B) PB NPs, with (light) and without (dark) laser irradiation. (C and D) Treatment of *S. aureus* (SA) with increasing concentrations of (C) CHPB and (D) PB NPs, with (light) and without (dark) laser irradiation.

The higher antibacterial potential of CHPB NPs was also ascertained from the time-dependent growth curves of *P. aeruginosa* (Fig. S5a, ESI†) and *S. aureus* (Fig. S5b, ESI†) upon treatment with various concentrations of PB and CHPB NPs, without and with laser irradiation. These data also showed the higher sensitivity of *P. aeruginosa* for CHPB NPs than that of *S. aureus*. This effect was also validated by a colony counting method involving *P. aeruginosa* cells treated with the PB and CHPB NPs, without and with light irradiation (Fig. S6, ESI†).

Since the surface of the CHPB NPs is modified with chitosan, a similar microbroth dilution assay was performed with equivalent amounts of chitosan alone, up to a treatment concentration of 175 μg ml^{-1}, against *P. aeruginosa* to examine the antibacterial influence of chitosan alone. The result displayed that chitosan alone at this treatment concentration has insignificant antibacterial activity (Fig. S7, ESI†). Indeed, the literature supports that chitosan is known for its inherent broad-spectrum antimicrobial action, with typical MIC values above a concentration of 0.1% w/v.[33,47–50] In our case, we have used a maximum chitosan concentration of 0.02% w/v for coating the nanoparticle surface. This result indicates that the enhanced antibacterial effect of CHPB over PB NPs is due to the increased interaction at the nanoparticle–bacteria interface for the former owing to the chitosan coating, rather than the added antibacterial effect of chitosan. The likely mechanism is that chitosan-coating reverses the surface charge of the otherwise anionic PB core, leading to its electrostatic interaction with the anionic bacterial cell membrane. This mechanism not only supports the higher antibacterial activity of CHPB over PB NPs, but also the enhanced vulnerability of the Gram-negative bacteria *P. aeruginosa* over that of the Gram-positive *S. aureus.* The outer membrane of Gram-negative bacteria is more anionic owing to the presence of phosphate and pyrophosphate groups, as compared to the less anionic polysaccharides and teichoic acid groups present on the outer membrane of Gram-positive bacteria.[47–50] This explains the comparatively higher electrostatic interaction and antibacterial potential of the cationic CHPB nanoparticles with *P. aeruginosa* over that of *S. aureus.* Similar observations with other nanoparticles have been reported in the literature.[32–34]

Mechanistic study of photo induced antibacterial effect of the nanoparticles

Four types of assays were conducted to evaluate the mechanism of antibacterial action of the NPs.

Metabolic arrest

Resazurin or Alamar dye is a purple non-fluorescent dye that gets converted to its pink fluorescent form resofurin by metabolically active cells. The reduction of resazurin is only catalyzed by functionally active enzymes and thus is possible only in viable cells. Fig. 6A and B shows that the degree of reduction of resazurin is inversely proportional to the concentration of the PB and CHPB NPs, which further reduced when irradiated with laser of wavelength 635 nm. The gradual decline in metabolic activity upon interaction with PB and CHPB NPs clearly suggests that *P. aeruginosa* and *S. aureus* lose their cellular integrity, which in turn affected their metabolism.

Intracellular ROS dependent oxidative stress

It is a well-known fact that during the basic metabolism of bacterial cells, there is production of highly reactive species called as reactive oxygen species (ROS), such as free radicals, superoxides, *etc.*; however, these generated ROS are counter balanced by various free radical scavenging enzymes.[18,25] The photothermal effect induced by laser irradiation can cause higher levels of ROS generation, which becomes toxic to the cell and causes irreversible cell damage and gradually cell death. To investigate whether PB and CHPB NPs, with and without laser irradiation, can enhance the production of ROS, we measured intracellular ROS levels of untreated and nanoparticle treated *P. aeruginosa* and *S. aureus* using DCFH-DA fluorometric assay. From Fig. 6C and D, it can be concluded that an increase in the concentration of the nanoparticles is directly proportional to the fluorescence intensity of the reduced form of dichlorofluorescein (DCF), indicative of intracellular ROS production as compared to untreated cells. As predicted, the ROS production increased when the nanoparticle-treated *P. aeruginosa* and *S. aureus* cells were irradiated with laser light due to hyperthermia produced by the PB core.

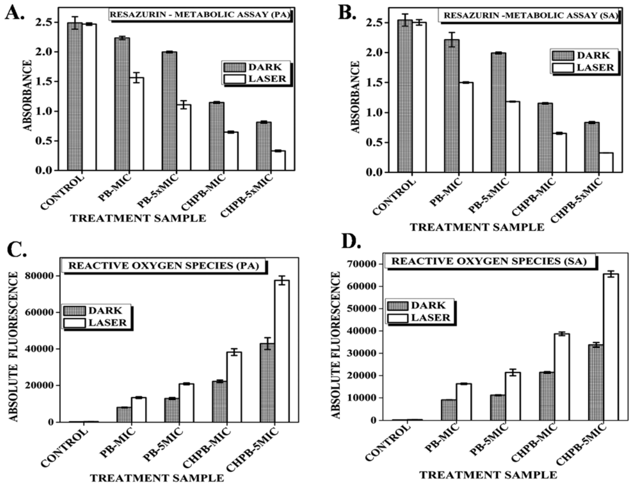

Fig. 6 Metabolic arrest studied through (A and B) Resazurin assay of (A) *P. aeruginosa* (PA) and (B) *S. aureus* (SA) treated with CHPB and PB NPs, without (dark) and with (light) laser irradiation. (C and D) The increase in oxidative stress of (C) *P. aeruginosa* and (D) *S. aureus* upon treatment with CHPB and PB NPs, without (dark) and with (light) laser irradiation.

Loss of membrane permeability

The passage of inflow or outflow of substances across the bacterial cell is regulated through a hydrophobic bilayered, selectively permeable membrane.[50] Any kind of disorganization of the membrane causes cell death. The ability of the synthesized PB and CHPB NPs to cause bacterial membrane damage was investigated using propidium iodide (PI) assay. Live bacterial cells are impermeable to PI, but it can enter cells with a damaged membrane and intercalate with nucleic acids, therein producing strong red fluorescence. Therefore, enhanced fluorescence indicates a higher loss of membrane permeability. *P. aeruginosa* and *S. aureus* cells were treated with their respective MIC concentrations of PB and CHPB NPs, with and without light treatment, and then incubated with PI. Fig. 7A and B shows an increase in PI fluorescence with increasing concentrations of PB and CHPB NPs, which further enhanced upon light irradiation. Furthermore, the membrane permeation effect of CHPB NPs was much more prominent than that of PB NPs, thus confirming the higher bactericidal effect of CHPB NPs. The presence of a positively charged chitosan coating on the CHPB NPs is expected to lead to a faster interaction at the nanoparticle–bacteria interface *via* strong electrostatic force, thus accelerating membrane destabilization.

Protein leakage

Furthermore, to validate the loss of membrane integrity, we carried out protein leakage assay on *P. aeruginosa* and *S. aureus* cells treated with PB and CHPB NPs. The results obtained showed a dose dependent increase in protein leakage with respect to untreated cells for both the NPs, with a further increase upon light activation, as shown in Fig. 7C and D. This result corroborates previous findings, thus confirming a higher compromise of bacterial membrane leading to more leaching of intracellular proteins when cells are treated with CHPB NPs.

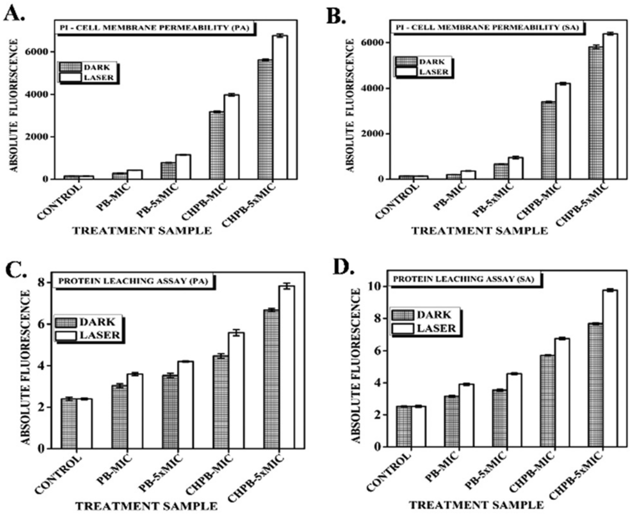

Fig. 7 Evaluation of bacterial membrane damage by (A and B) PI uptake assay of (A) *P. aeruginosa* (PA) and (B) *S. aureus* (SA), treated with PB and CHPB NPs, without (dark) and with (light) laser irradiation. (C and D) protein leaching assay of (C) *P. aeruginosa* and (D) *S. aureus* treated with PB and CHPB NPs, without (dark) and with (light) laser irradiation.

Transmission electron microscopy (TEM) analysis of bacterial cells treated with the NPs

TEM analysis of untreated and treated (with CHPB and PB NPs, at their MIC values) bacterial cells revealed surface attachment of the nanoparticles (Fig. S8, ESI†) along with structural membrane damage (Fig. S9 and S10, ESI†), supporting previous results. From Fig. S8, ESI,† it can be ascertained that both PB and CHPB NPs bind to the surface of both PA and SA. However, whether CHPB NPs bind with more affinity than PB NPs could not be conclusively evaluated from these data. The untreated *P. aeruginosa* shows a continuous smooth membrane structure with a rod shaped configuration, both without (Fig. S9A, ESI†) and with (Fig. S9C, ESI†) light treatment. However, upon CHPB NP treatment, the cells displayed compromised, ruptured membrane structures and leaked intracellular contents (Fig. S9B and D, ESI†). Similar results were obtained for *S. aureus*, where the usually smooth and near-spherical morphology of the cells became distorted and damaged upon CHPB NP treatment, which further worsened upon light irradiation (Fig. S10A–D, ESI†). The results supported the previous findings of extensive bacterial cell death resulting from membrane damage and loss of structural integrity following treatment with CHPB NPs and light.

Interaction of CHPB NPs with mammalian cells

To probe the general biocompatibility of the CHPB NPs, we evaluated their effect towards the mammalian cell line HEK-293. The result shows that the CHPB NPs did not show any toxicity up to a concentration of 150 $\mu g\ ml^{-1}$ in the dark (Fig. S11, ESI†). It should be noted that at this concentration of CHPB NPs, substantial toxicity was observed for both the bacterial cells, even without light irradiation. This result shows that despite being generally non-toxic, the CHPB NPs show potent antibacterial effects, particularly upon light activation.

Conclusions

The key conclusions from this work are the following: (a) PB NPs have an inherent antibacterial effect owing to their peroxidase-like behavior, (b) light-activation enhances their antibacterial activity *via* the added photothermal effect, and (c) chitosan coating further increases the antibacterial potential of these nanoparticles. Although chitosan is known to exert some antibacterial activity itself (at much higher concentrations than that used in this nanoparticle coating), we believe that in our investigation, the polymeric coating is simply enhancing the affinity of the CHPB NPs towards the bacterial cells. CHPB NPs have a smaller size and cationic charge, while the anionic PB NPs are comparatively larger in size. Both these factors should help the CHPB NPs attach and infiltrate the bacterial cells better. Upon attachment, the CHPB NPs cause depolarization of the membrane surface, followed by severe surface deformation as elucidated from the TEM images. The particles further infiltrate the cells and cause expulsion of the cytoplasmic contents and membrane damage followed by metabolic inactivation. Inside the cells, the particles cause a severe increase in ROS production due to their peroxidase-like activity, along with local hyperthermia upon light activation. The localized hyperthermia and ROS produced in the presence of the nanoparticles can also aid in cell membrane rupture and protein denaturation. Thus, an increase in oxidative stress along with the membrane disruption due to the chitosan coating in the CHPB nanoparticles collectively participated in the inhibition of growth of the bacteria. The Gram-negative *P. aeruginosa* bacteria are more sensitive than the Gram-positive *S. aureus* bacteria owing to the higher anionic membrane density in the former. Overall, the CHPB NPs with a positive surface charge and enhanced ablation effect of local hyperthermia with a low power laser show great potential as a targeted photothermal nano-agent, opening up future possibilities for the treatment of various bacterial infections.

Conflicts of interest

The authors declare no conflict of interest.

Acknowledgements

This study was mainly supported by a research grant from Nanomission, Department of Science and Technology, Government of India. NC is thankful to the Center for Scientific and Industrial Research (CSIR), Government of India, for providing fellowship support. The authors also acknowledge the laboratory and Instrumentation facilities from the University of Delhi and CSIR-IGIB for conducting various experiments.

Notes and references

1 S. Lehtinen, F. Blanquart, M. Lipsitch and C. Fraser, *PLoS Pathog.*, 2019, **15**, e1007763.
2 S. B. Levy, *Lancet*, 1982, **320**, 83–88.

3 S. B. Levy and M. Bonnie, *Nat. Med.*, 2004, **10**, 122–129.

4 A. J. Huh and Y. J. Kwon, *J. Controlled Release*, 2011, **156**, 128–145.

5 A. M. Allahverdiyev, K. V. Kon, E. S. Abamor, M. Bagirova and M. Rafailovich, *Expert Rev. Anti-Infect. Ther.*, 2011, **9**, 1035–1052.

6 U. Shimanovich and A. Gedanken, *J. Mater. Chem. B*, 2016, **4**, 824–833.

7 O. C. Farokhzad and R. Langer, *ACS Nano*, 2009, **3**, 16–20.

8 G. Chen, I. Roy, C. Yang and P. N. Prasad, *Chem. Rev.*, 2016, **116**, 2826–2885.

9 D. Jaque, L. Martínez-Maestro, B. del Rosal, P. Haro-Gonzalez, A. Benayas, J. L. Plaza, E. Martín-Rodríguez and J. García-Solé, *Nanoscale*, 2014, **6**, 9494–9530.

10 C. Urban, A. S. Urban, H. Charron and A. Joshi, *Transl. Cancer Res.*, 2013, **2**, 292–308.

11 A. C. Burduşel, O. Gherasim, A. M. Grumezescu, L. Mogoantă, A. Ficai and E. Andronescu, *Nanomaterials*, 2018, **8**, 681.

12 N. Durán, M. Durán, M. B. de Jesus, A. B. Seabra, W. J. Fávaro and G. Nakazato, *Nanomedicine*, 2016, **12**, 789–799.

13 E. Ugwoke, S. O. Aisida, A. A. Mirbahar, M. Arshad, I. Ahmad, T.-k. Zhao and F. I. Ezema, *Surf. Interfaces*, 2020, **18**, 100419.

14 R. Miethling-Graff, R. Rumpker, M. Richter, T. Verano-Braga, F. Kjeldsen, J. Brewer, J. Hoyland, H. G. Rubahn and H. Erdmann, *Toxicol. In Vitro*, 2014, **28**, 1280–1289.

15 S. Gaillet and J. M. Rouanet, *Food Chem. Toxicol.*, 2015, **77**, 58–63.

16 A. Panáček, L. Kvítek, M. Smékalová, R. Večeřová, M. Kolář, M. Röderová, F. Dyčka, M. Šebela, R. Prucek, O. Tomanec and R. Zbořil, *Nat. Nanotechnol.*, 2018, **13**, 65–71.

17 T. Kang, Y. G. Kim, D. Kim and T. Hyeon, *Coord. Chem. Rev.*, 2020, **403**, 213092.

18 Y. Huang, J. Ren and X. Qu, *Chem. Rev.*, 2019, **119**, 4357–4412.

19 G. Fang, W. Li, X. Shen, J. M. Perez-Aguilar, Y. Chong, X. Gao, Z. Chai, C. Chen, C. Ge and R. Zhou, *Nat. Commun.*, 2018, **9**, 129.

20 H. Wang, P. H. Li, D. Q. Yu, Y. Zhang, Z. Z. Wang, C. Q. Liu, H. Qiu, Z. Liu, J. S. Ren and X. G. Qu, *Nano Lett.*, 2018, **18**, 3344–3351.

21 W. Y. Yin, J. Yu, F. T. Lv, L. Yan, L. R. Zheng, Z. J. Gu and Y. L. Zhao, *ACS Nano*, 2016, **10**, 11000–11011.

22 J. Xi, G. Wei, Q. Wu, Z. Xu, Y. Liu, J. Han, L. Fan and L. Gao, *Biomater. Sci.*, 2019, **7**, 4131–4141.

23 M. Shokouhimehr, E. S. Soehnlen, J. Hao, M. Griswold, C. Flask, X. Fan, J. P. Basilion, S. Basu and S. D. Huang, *J. Mater. Chem.*, 2010, **20**, 5251–5259.

24 Z. Qin, Y. Li and N. Gu, *Adv. Healthcare Mater.*, 2018, **7**, 1800347.

25 W. Zhang, S. Hu, J. J. Yin, W. He, W. Lu, M. Ma, N. Gu and Y. Zhang, *J. Am. Chem. Soc.*, 2016, **138**, 5860–5865.

26 W. Zhang, D. Ma and J. Du, *Talanta*, 2014, **120**, 362–367.

27 G. Fu, W. Liu, S. Feng and X. Yue, *Chem. Commun.*, 2012, **48**, 11567–11569.

28 G. Dacarro, A. Taglietti and P. Pallavicini, *Molecules*, 2018, **23**, 1414.

29 G. Dacarro, P. Grisoli, M. Borzenkov, C. Milanese, E. Fratini, G. Ferraro, A. Taglietti and P. Pallavicini, *Supramol. Chem.*, 2017, **29**, 823–833.

30 H. Maaoui, R. Jijie, G. H. Pan, D. Drider, D. Caly, J. Bouckaert, N. Dumitrascu, R. Chtourou, S. Szunerits and R. Boukherroub, *J. Colloid Interface Sci.*, 2016, **480**, 63–68.

31 D. Zhao, S. Yu, B. Sun, S. Gao, S. Guo and K. Zhao, *Polymers*, 2018, **10**, 462.

32 S. K. Saha, P. Roy, M. K. Mondal, D. Roy, P. Gayen, P. Chowdhury and S. P. S. Babu, *Carbohydr. Polym.*, 2017, **157**, 1666–1676.

33 M. Arakha, S. Pal, D. Samantarrai, T. K. Panigrahi, B. C. Mallick, K. Pramanik, B. Mallick and S. Jha, *Sci. Rep.*, 2015, **5**, 14813.

34 S. Roy, A. Mondal, V. Yadav, A. Sarkar, R. Banerjee, P. Sanpui and A. Jaiswal, *ACS Appl. Bio Mater.*, 2019, **2**, 2738–2755.

35 Q. Zhang, L. Zhang and J. Li, *Electrochim. Acta*, 2008, **53**, 3050–3055.

36 B. Folch, J. Larionova, Y. Guari, K. Molvinger, C. Luna, C. Sangregorio, C. Innocenti, A. Caneschi and C. Guérin, *Phys. Chem. Chem. Phys.*, 2010, **12**, 12760–12770.

37 X. Da Li, X. L. Liang, F. Ma, L. J. Jing, L. Lin, Y. B. Yang, S. S. Feng, G. L. Fu, X. L. Yue and Z. F. Dai, *Colloids Surf., B*, 2014, **123**, 629–638.

38 H. H. Zhang, G. H. Chen, H. Zhang, H. L. Cong and B. Yu, *Ferroelectrics*, 2018, **529**, 100–104.

39 F. Yu, Y. Huang, A. J. Cole and V. C. Yang, *Biomaterials*, 2009, **30**, 4716–4722.

40 H. Possel, H. Noack, W. Augustin, G. Keilhoff and G. Wolf, *FEBS Lett.*, 1997, **416**, 175–178.

41 S. N. Rampersad, *Sensors*, 2012, **12**, 12347–12360.

42 O. Ernst and T. Zor, *J. Visualized Exp.*, 2010, **38**, 1918.

43 P. Tyagi, M. Singh, H. Kumari, A. Kumari and K. Mukhopadhyay, *PLoS One*, 2015, **10**, e0121313.

44 A. M. Farah, N. D. Shooto, F. T. Thema, J. S. Modise and E. D. Dikio, *Int. J. Electrochem. Sci.*, 2012, **7**, 4302–4313.

45 Z. Li, Y. Hu, T. Jiang, K. A. Howard, Y. Li, X. Fan, Y. Sun, F. Besenbacher and M. Yu, *Part. Part. Syst. Charact.*, 2016, **33**, 53–62.

46 T. Uemura, M. Ohba and S. Kitagawa, *Inorg. Chem.*, 2004, **43**, 7339–7345.

47 R. C. Goy, D. de Britto and O. B. G. Assis, *Polimeros*, 2009, **19**, 241–247.

48 A. Anitha, V. V. Divya Rani, R. Krishna, V. Sreeja, N. Selvamurugan, S. V. Nair, H. Tamura and R. Jayakumar, *Carbohydr. Polym.*, 2009, **78**, 672–677.

49 L. Qi, Z. Xu, X. Jiang, C. Hu and X. Zou, *Carbohydr. Res.*, 2004, **339**, 2693–2700.

50 L. Y. Zheng and J. F. Zhu, *Carbohydr. Polym.*, 2003, **54**, 527–530.